# Measured load spectra of the bearing in high-speed train gearbox under different gear meshing conditions

Yu Hou[1] · Xi Wang[1] · Shouguang Sun[1] · Hongbo Que[2] · Rubing Guo[2] · Xinhai Lin[2] ·
Siqin Jin[2] · Chengpan Wu[2] · Yue Zhou[1] · Xiaolong Liu[1]

**Abstract**   The load spectrum is a crucial factor for assessing the fatigue reliability of in-service rolling element bearings in transmission systems. For a bearing in a high-speed train gearbox, a measurement technique based on strain detection of bearing outer ring was used to instrument the bearing and determine the time histories of the distributed load in the bearing under different gear meshing conditions. Accordingly, the load spectrum of the total radial load carried by the bearing was compiled. The mean value and class interval of the obtained load spectrum were found to vary non-monotonously with the speed and torque of gear meshing, which was considered to be caused by the vibration of the shaft and the bearing cage. As the realistic service load input of bearing life assessment, the measured load spectrum under different gear meshing conditions can be used to predict gearbox bearing life realistically based on the damage-equivalent principle and actual operating conditions.

**Keywords**   Gearbox bearing · High-speed train · Strain response · Load spectra · Gear meshing conditions

## 1 Introduction

Over the past decade, the high-speed railway has become an indispensable mode of transportation worldwide, with outstanding features of safety, high efficiency, comfort and reduced-pollution [1]. The development of railway passenger transportation requires high operational safety and reliability of high-speed trains, where the accurate and realistic condition monitoring and life prediction of structural components under actual service conditions are necessary. The gearbox assembly is a key transmission component of a high-speed train traction system. It connects the traction motor with the axle and transmits the motor torque to the axle by a pair of helical gears. As a link between the shafts and the gearbox housing, the rolling element bearing allows the transmission of forces between the gearbox system and its environment while guiding the rotational movement of the shafts. Its operating status plays a critical role in the safety and reliability of high-speed trains, and health monitoring of the rolling element bearing in the gearbox is important.

To in-situ monitor the operating status of drivetrain bearings, the temperature, vibration and sound were measured in most of the existing monitoring technologies [2–4], and many studies focus on the fault diagnosis method of the bearings [5–7]. However, abnormal temperature, vibration and sound are the symptom of bearing failure [4], not the cause of bearing failure. The monitoring of temperature, vibration and sound works only when the bearing fault appears, which is lagging for the health monitoring and reliability assessment of drivetrain bearings. Differing from temperature, vibration and sound, the mechanical parameter such as the dynamic load applied on the bearing is considered to be an important cause of bearing fatigue failure [8–10]. Thus, for life prediction and reliability assessment of bearings in a transmission system under service conditions, the monitoring of bearing load is significant and should be paid attention to. Besides, it is well established that fatigue response may be very sensitive to the specifics of the dynamic loading encountered [11]. In the gearbox, gears and bearings are kinetically coupled components and interact with each other as the gear meshing forces are supported by the bearings.

During the operation of trains, the gearbox bearing in high-speed trains experiences complex and various load conditions under the influence of internal excitation from gear meshing [12] and external excitation from wheel–rail contact [13, 14]. Therefore, realistic load spectra under different service conditions are required to assess the fatigue reliability and to demonstrate the in-service integrity of gearbox bearings. The indications of bearing health based on monitoring dynamic bearing load can then be used to organize effective maintenance and minimize unplanned downtime.

Both numerical methods and measurement techniques were developed to understand the bearing load in a transmission system under service conditions. Evans et al. [14] presented a multistep dynamic analysis process for linking railcar vibration conditions to bearing component motions and obtained the bearing load numerically. Wang et al. [15, 16] developed a comprehensive vehicle–track coupled dynamics model and investigated the influence of wheel–rail excitation on the axle box bearing load. Liu et al. [17, 18] discussed the effect of surface waviness and rotor eccentricity on the motor bearing load by using a locomotive–track spatially coupled dynamics model with detailed traction power transmissions. To measure the load of the tapered roller bearing in the wind turbine gearbox, four equally spaced axial grooves were machined in their outer rings and eight strain gauge pairs were used by Keller and Guo et al. [19–22]. However, this modification of the bearing changed the original load distribution within the bearing, which led to an amount of uncertainty higher than the desired in the estimation of the measured bearing radial load [19, 22]. Recently, new ultrasonic reflectometry techniques have been implemented by Chen et al. [23] and Nicholas et al. [24] to measure the contact load in a field operational wind turbine gearbox bearing. Nevertheless, a high sampling frequency of 100 MHz is required for ultrasonic measurement, which results in a large amount of data accumulation and difficulty in long-term monitoring. Overall, although the bearing load conditions have been numerically or experimentally studied, few works applied to the in-situ monitoring of bearing load in high-speed train gearbox and no load spectrum was compiled and presented in the literature due to the limitations of existing methods.

Previously, for in-situ measurement of contact load distribution within rolling element bearings with good accuracy, a new method based on strain measurement has been successfully developed, implemented and applied without any modifications to the bearing itself [25, 26]. In the current study, instrumentation based on this approach is added to a bearing in high-speed train gearbox. The load spectra of the gearbox bearing are measured and compiled. The effect of the gear meshing conditions on the load spectra of the bearing is analyzed. Furthermore, the application of the measured load spectrum in bearing life assessment is discussed.

## 2 Instrumentation and methodology

This work focuses on a single-stage 650 kW gearbox with a ratio of 1:2.429 from the CRH380B electric multiple units (EMU) as shown in Fig. 1. This configuration of the gearbox represents a majority of real-scale high-speed train gearboxes. The high-speed shaft is supported with two cylindrical roller bearings and one four-point contact ball bearing. The cylindrical roller bearing NU214ECML from the wheel side was selected as the test bearing. Key specifications of the test bearing are shown in Table 1. This cylindrical roller bearing reacts against the radial load whose direction and amplitude depend on and vary with the operational conditions of the gear meshing [20]. Thus, to monitor the dynamic radial load of the bearing, it is necessary to measure the
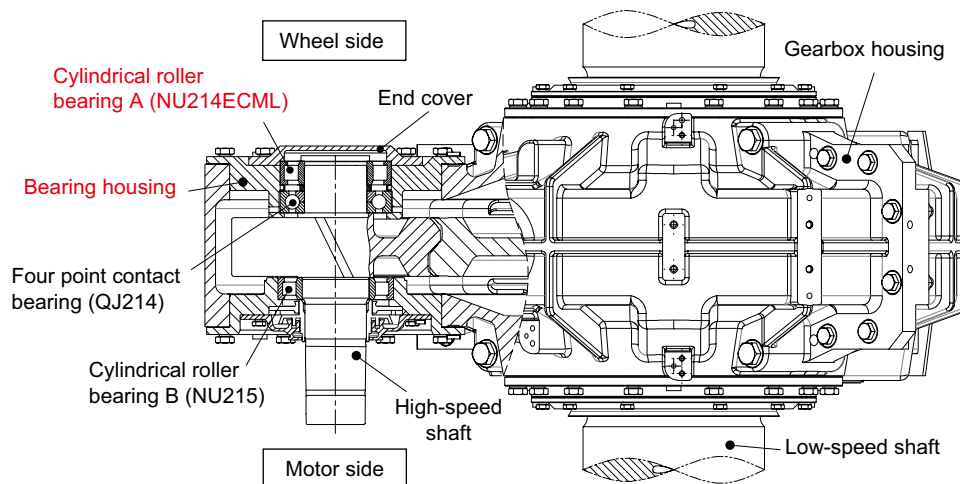


**Fig. 1** Test gearbox structure and high-speed shaft bearing configuration

**Table 1** Specifications of the instrumented bearing

| Bearing model | SKF NU214ECML |
|---|---|
| Bearing outside diameter | 125 mm |
| Bearing bore diameter | 70 mm |
| Roller diameter | 15 mm |
| Roller length | 14 mm |
| Number of rollers | 17 |

contact load distribution within the bearing. For detecting the distribution of roller–raceway contact loads, the gearbox NU214ECML bearing was instrumented with strain gauges as shown in Fig. 2. Totally 17 pieces of strain gauges in full-bridge arrangements were bonded on the outer surface of the bearing [25] with a LOCTITE 495 instant adhesive and sealed with a 704 silicone rubber. Full-bridge arrangements of strain gauges were used here to eliminate the effect of temperature variations. The upper operating temperatures of the adhesive and rubber are 120 and 250 °C, respectively, which are sufficiently above the expected operational temperature of the bearing (< 80 °C). The test positions were numbered counterclockwise from 1 to 17 with the point No.1 located at the top of the bearing when the instrumented bearing was assembled in the gearbox.

The test bearing is installed in a bearing housing as shown in Fig. 3. During the assembly, the bearing housing is connected with instrumented bearing under an interference fit and then assembled on the gearbox by bolts under a clearance fit. Before the experiment, the original bearing housing was modified; 17 notches were introduced by computerized numerical control (CNC) milling and evenly distributed on the inner surface of the bearing housing [25]. Each notch had the same size with axial length of 19 mm, circumferential length of 11 mm, and radial depth of 2 mm (Fig. 3d). Each strain gauge location of the instrumented
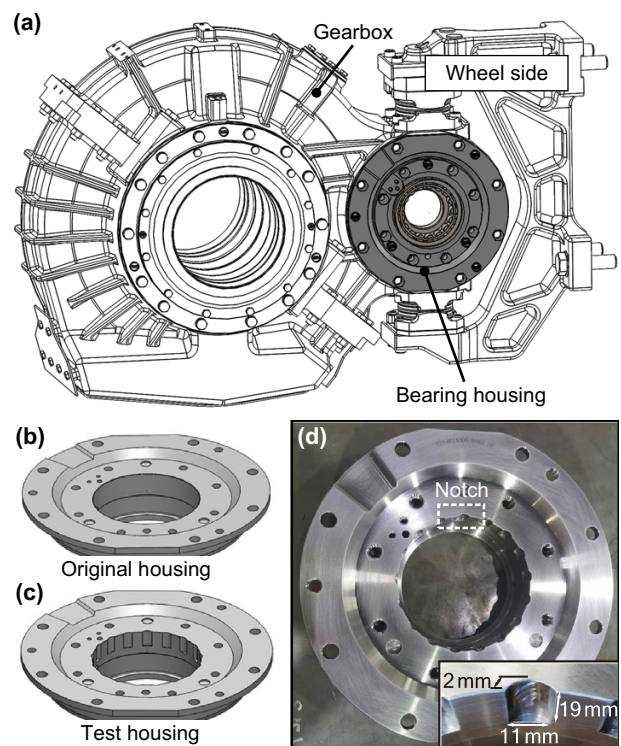


**Fig. 3** Position and instrumentation of the test bearing housing: **a** position of the test bearing housing; **b** original housing; **c** modified housing; **d** photo of the modified housing and its notches

bearing corresponds to the center of a notch of the instrumented housing during the fit process.

By instrumenting the bearing and its housing, once a calibration matrix $K_{\alpha\_\beta}$ is obtained and the real-time strain distribution $\varepsilon_\alpha(t)$ is measured, the real-time load distribution $F_\beta(t)$ within the bearing can be determined as follows [25]:
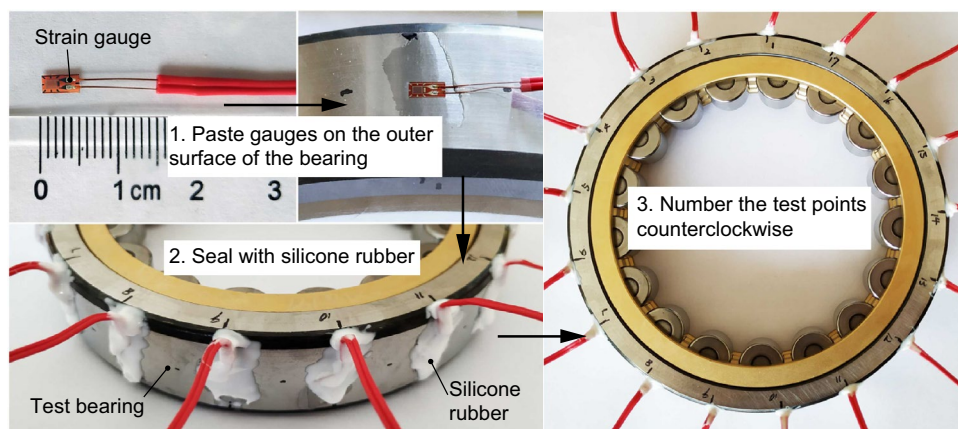


**Fig. 2** Bearing instrumentation process

$$F_\beta(t) = K_{\alpha\_\beta}^{-1} \cdot \varepsilon_\alpha(t), \tag{1}$$

where the subscripts $\alpha$ and $\beta$ represent the sensing location number (1, 2, …, 17); elements of the calibration matrix $K_{\alpha\_\beta}$, denoted by $k_{\alpha\_\beta}$, represent the strains at the sensing location $\alpha$ due to a unit force applied at sensing location $\beta$ when all other loads are zero. Then, according to the relationship between the total radial load and the load distribution [27], the real-time total radial load $F_r(t)$ can be calculated by

$$F_r(t) = \sum_{\beta=1}^{Z} F_\beta(t) \cdot \cos \psi_\beta, \tag{2}$$

where $\psi_\beta$ represents the angle between the distributed load $F_\beta$ and the maximum roller–raceway contact load; $Z$ is the number of rollers in the test bearing and equal to 17 in this paper.

## 3 Experiment

The experiment was divided into two steps. First, the assembly of instrumented bearing and its housing was loaded in an MTS test machine with a specially designed loading fixture to determine the calibration matrix $K_{\alpha\_\beta}$. Second, the instrumented bearing and housing were installed in the gearbox and a test bench of high-speed train traction system was used to measure the dynamic distributed strain signals of the test bearing under different gear meshing conditions. An eDAQ (serial number 5448) from HBM Company was adopted as the strain acquisition equipment in the whole experiment. The sampling frequency was, respectively, set to 2.5 kHz in the first step and 20 kHz in the second step.

### 3.1 Determination of the calibration matrix

The experimental setup for determining the calibration matrix of the test bearing is shown in Fig. 4. As shown in Fig. 4a, the whole setup consists of a base, two supports, a shaft, bearings, bearing housing and a polygonal loading
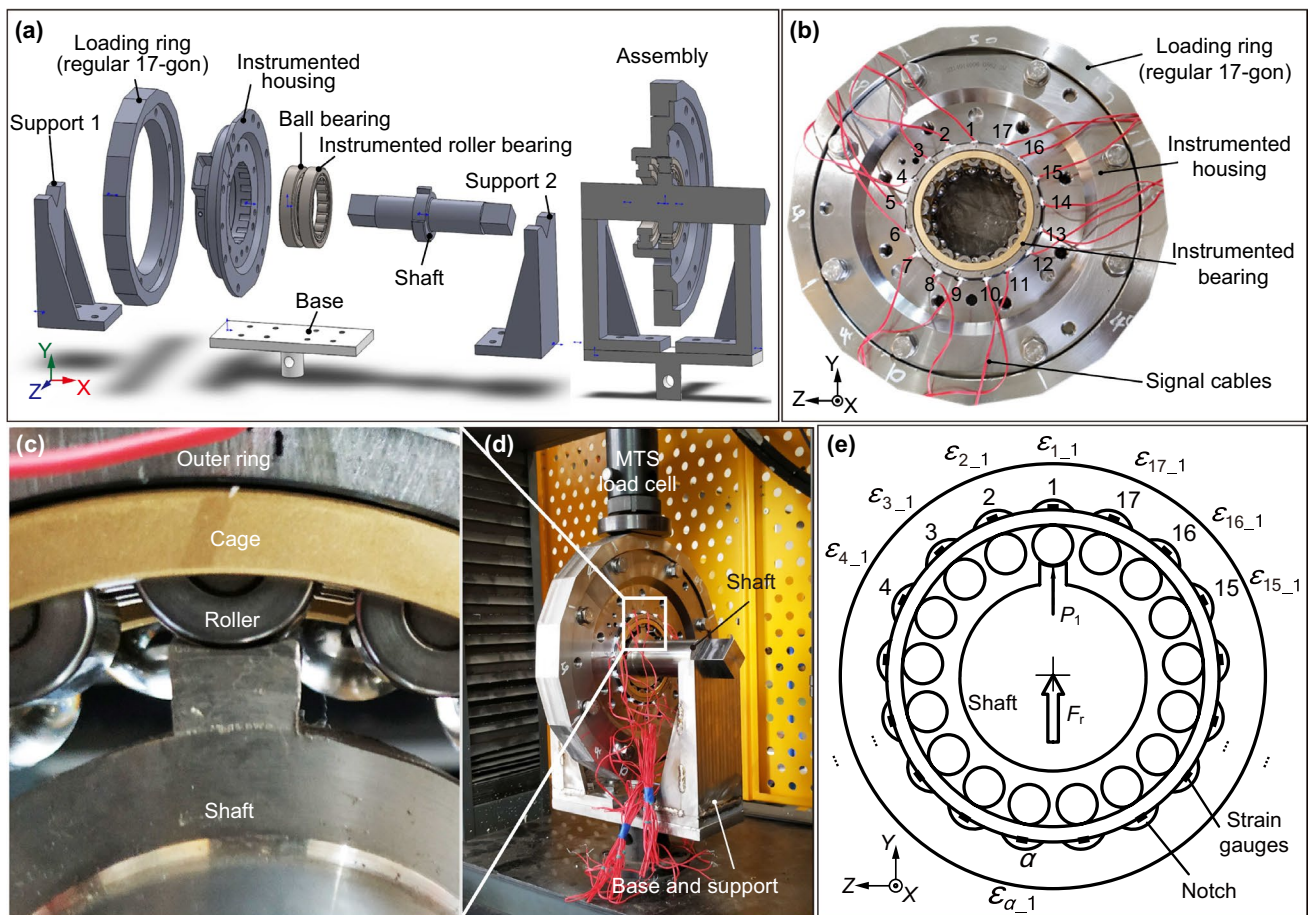


**Fig. 4** **a**–**d** Experimental setup for determining the calibration matrix and **e** the schematic diagram of the test of the calibration matrix components $k_{\alpha\_1}$

Springer

Rail. Eng. Science (2023) 31(1):37–51

ring. A regular 17 polygon fixture was designed and assembled with the instrumented bearing housing by bolts as shown in Fig. 4b. The ball bearing and the instrumented roller bearing were fitted in the housing as usual. A shaft was designed with a concave protrusion to apply the force only on a specific sensing position as shown in Fig. 4c. The setup was installed in an MTS test machine as shown in Fig. 4d.

The calibration matrix components $k_{\alpha\_\beta}$ can be obtained as follows:

$$k_{\alpha\_\beta} = \frac{\Delta\varepsilon_{\alpha\_\beta}}{\Delta P_\beta}, \tag{3}$$

where $\varepsilon_{\alpha\_\beta}$ is the measured strain at the test point No. $\alpha$ when the load $P_\beta$ is applied to the test point No. $\beta$. As shown in Fig. 4e, when the load $P_1$ is applied to the test point No. 1, $\varepsilon_{\alpha\_1}$ ($\alpha$ represents 1 to 17) can be measured. The applied load increases from 0 to 9 kN with the increment of 1 kN

during a test. With the increase of $P_1$, the change of $\varepsilon_{\alpha\_1}$ is recorded. Thus, the calibration matrix components $k_{\alpha\_1}$ can be obtained by Eq. (3). All the values of applied loads in this experiment have already removed the part of self-weight. The shaft is kept static to ensure that the loading roller is located at the top and in the line of the loading direction. Other calibration components $k_{\alpha\_\beta}$ can be obtained similarly by rotating the corresponding sensing location to the top position. Finally, a $17 \times 17$ calibration matrix $\boldsymbol{K}_{\alpha\_\beta}$ can be determined.

## 3.2 Measurement of dynamic strain distribution under gear meshing

After the calibration, the assembly of instrumented bearing and its housing was removed from the calibration setup and mounted in the test gearbox; 17 small holes were machined on the end cover of the gearbox for leading out the signal
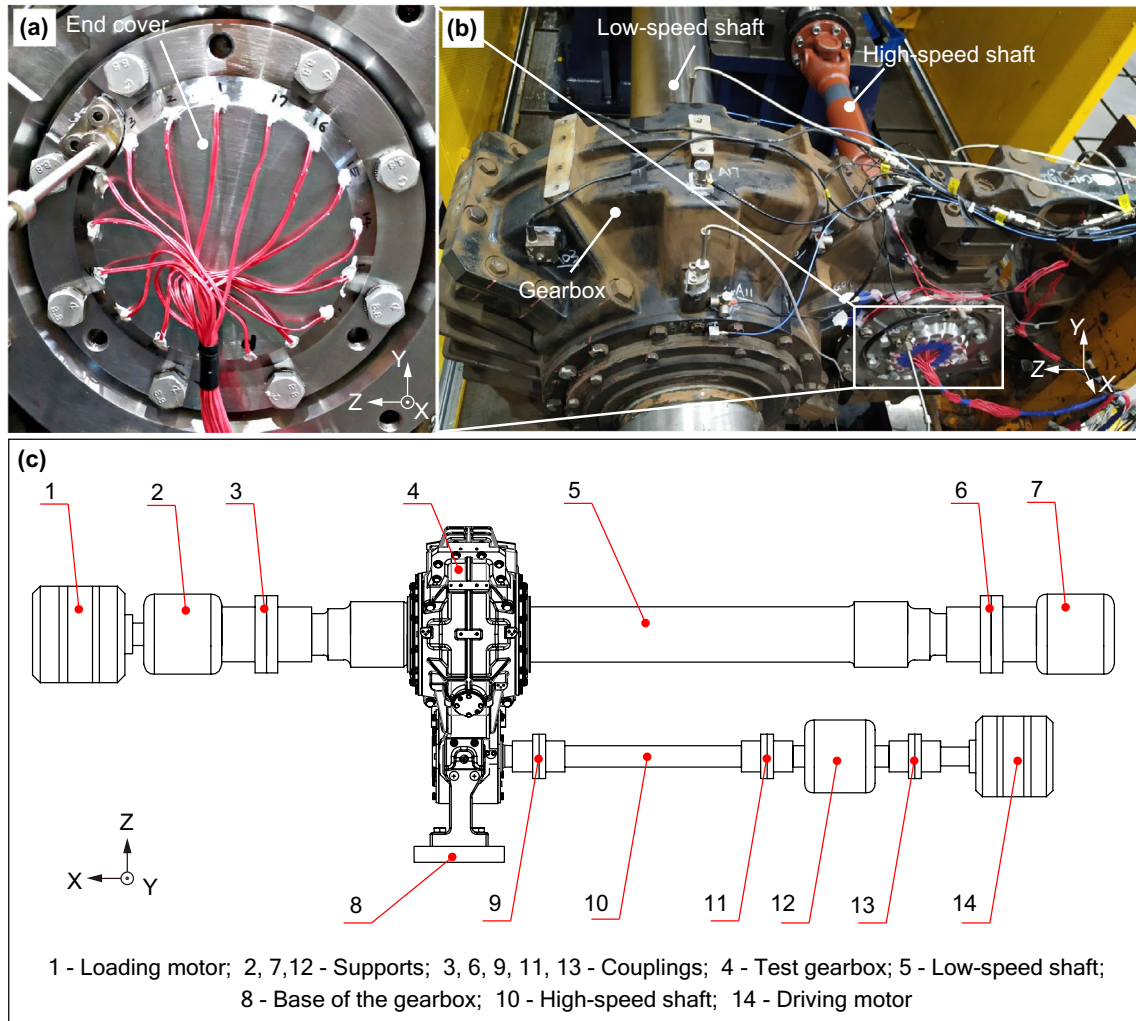


**Fig. 5** High-speed train traction system test bench: **a** layout of the signal cables; **b** photo of the test bench; **c** schematic diagram of the test bench

cables of strain gauges and sealed with the silicone rubber to prevent the lubricant leakage as shown in Fig. 5a. Then, the test gearbox was installed in the test bench of the high-speed train traction system as shown in Fig. 5b. Figure 5c shows the construction and arrangement of the test bench. The maximum input speed of the test bench is 6500 rpm and the maximum load torque is 7900 N·m.

The experiment was conducted in two phases and two series of gear meshing conditions were, respectively, examined based on the actual working conditions of the high-speed train traction system. In the first phase, constant-speed operations were conducted throughout a range of input torque levels. The high-speed shaft rotated stably at 1550 rpm (corresponding to the train speed of 100 km/h) in this phase. In the second phase, several field-representative input speeds were conducted while the input torque was fixed at 1000 N·m. During the tests, the rotational direction of the high-speed shaft was clockwise (looking from the wheel side) and the high-speed shaft bearing was lubricated with 75 W-90 gear oil.

## 4 Results and discussion

### 4.1 Calibration matrix

Figure 6 shows the real-time load applied by the MTS load cell and typical results of the strain signals from the calibration test when the test point No. 1 is loaded. The radial load was applied with a rate of 25 N/s and kept at each target value for 10 s. It can be found that $\varepsilon_{1\_1}$ is positive and linearly increases with the load $P_1$, while $\varepsilon_{2\_1}$ and $\varepsilon_{17\_1}$ are negative and decrease with the increase of the load $P_1$. It indicates that, when the load is applied on the test point No. 1, the outer surface deformation of sensing location No. 1 is in tension while the sensing locations No. 2 and No. 17 are in compression. Among the strains of test points which were farther from the test point No. 1, $\varepsilon_{3\_1}$, $\varepsilon_{4\_1}$, $\varepsilon_{5\_1}$ and $\varepsilon_{16\_1}$, $\varepsilon_{15\_1}$, $\varepsilon_{14\_1}$ are also positively correlated with the load applied on the test point No. 1, while $\varepsilon_{6\_1}$ and $\varepsilon_{13\_1}$ are nearly zero all the time. The other strain signals are also almost zero since they are far away from the loading point and they are not shown here.

According to Eq. (3), the ratios of $\Delta\varepsilon_{\alpha\_1}$ and $\Delta P_1$ were calculated and considered as the calibration matrix components $k_{\alpha\_1}$. Similar relationships between the measured values of strains $\varepsilon_{\alpha\_\beta}$ ($\beta \neq 1$) and the load $P_\beta$ ($\beta \neq 1$) were obtained and corresponding matrix components $k_{\alpha\_\beta}$ ($\beta \neq 1$) were calculated. Then, the $17 \times 17$ calibration matrix $K_{\alpha\_\beta}$ in this experiment was determined as

$K_{\alpha\_\beta} =$

$$
\begin{bmatrix}
0.08692 & -0.00228 & 0.00169 & 0.00115 & 0.00040 & 0 & 0 & 0 & 0 & 0 & 0 & 0 & 0 & 0.00086 & 0.00103 & 0.00202 & -0.00342 \\
-0.00250 & 0.08471 & -0.00421 & 0.00192 & 0.00146 & 0.00048 & 0 & 0 & 0 & 0 & 0 & 0 & 0 & 0 & 0.00059 & 0.00157 & 0.00172 \\
0.00216 & -0.00220 & 0.08837 & -0.00426 & 0.00261 & 0.00136 & 0.00071 & 0 & 0 & 0 & 0 & 0 & 0 & 0 & 0 & 0.00082 & 0.00093 \\
0.00184 & 0.00162 & -0.00326 & 0.08942 & -0.00503 & 0.00196 & 0.00134 & 0.00092 & 0 & 0 & 0 & 0 & 0 & 0 & 0 & 0 & 0.00060 \\
0.00073 & 0.00119 & 0.00187 & -0.00353 & 0.09488 & -0.00287 & 0.00253 & 0.00173 & 0.00110 & 0 & 0 & 0 & 0 & 0 & 0 & 0 & 0 \\
0 & 0.00065 & 0.00111 & 0.00176 & -0.00413 & 0.09538 & -0.00411 & 0.00210 & 0.00206 & 0.00066 & 0 & 0 & 0 & 0 & 0 & 0 & 0 \\
0 & 0 & 0.00038 & 0.00108 & 0.00184 & -0.00250 & 0.09026 & -0.00402 & 0.00266 & 0.00121 & 0.00083 & 0 & 0 & 0 & 0 & 0 & 0 \\
0 & 0 & 0 & 0.00053 & 0.00163 & 0.00154 & -0.00404 & 0.09302 & -0.00285 & 0.00214 & 0.00126 & 0.00072 & 0 & 0 & 0 & 0 & 0 \\
0 & 0 & 0 & 0 & 0.00085 & 0.00111 & 0.00205 & -0.00259 & 0.10034 & -0.00470 & 0.00166 & 0.00136 & 0.00089 & 0 & 0 & 0 & 0 \\
0 & 0 & 0 & 0 & 0 & 0.00071 & 0.00132 & 0.00201 & -0.00329 & 0.08609 & -0.00378 & 0.00125 & 0.00146 & 0.00061 & 0 & 0 & 0 \\
0 & 0 & 0 & 0 & 0 & 0 & 0.00092 & 0.00117 & 0.00160 & -0.00401 & 0.09296 & -0.00260 & 0.00183 & 0.00134 & 0.00065 & 0 & 0 \\
0 & 0 & 0 & 0 & 0 & 0 & 0 & 0.00037 & 0.00138 & 0.00163 & -0.00301 & 0.09093 & -0.00379 & 0.00188 & 0.00124 & 0.00090 & 0 \\
0 & 0 & 0 & 0 & 0 & 0 & 0 & 0 & 0.00083 & 0.00105 & 0.00167 & -0.00255 & 0.08533 & -0.00371 & 0.00251 & 0.00133 & 0.00039 \\
0.00046 & 0 & 0 & 0 & 0 & 0 & 0 & 0 & 0 & 0.00070 & 0.00131 & 0.00172 & -0.00319 & 0.08643 & -0.00453 & 0.00237 & 0.00105 \\
0.00110 & 0.000414 & 0 & 0 & 0 & 0 & 0 & 0 & 0 & 0 & 0.00060 & 0.00130 & 0.00201 & -0.00343 & 0.08260 & -0.00345 & 0.00182 \\
0.00146 & 0.00119 & 0.00044 & 0 & 0 & 0 & 0 & 0 & 0 & 0 & 0 & 0.00087 & 0.00156 & 0.00249 & -0.00301 & 0.09401 & -0.00374 \\
-0.00296 & 0.00125 & 0.00116 & 0.00070 & 0 & 0 & 0 & 0 & 0 & 0 & 0 & 0 & 0.00084 & 0.00153 & 0.00228 & -0.00287 & 0.09151 \\
\end{bmatrix}
. \quad (4)
$$
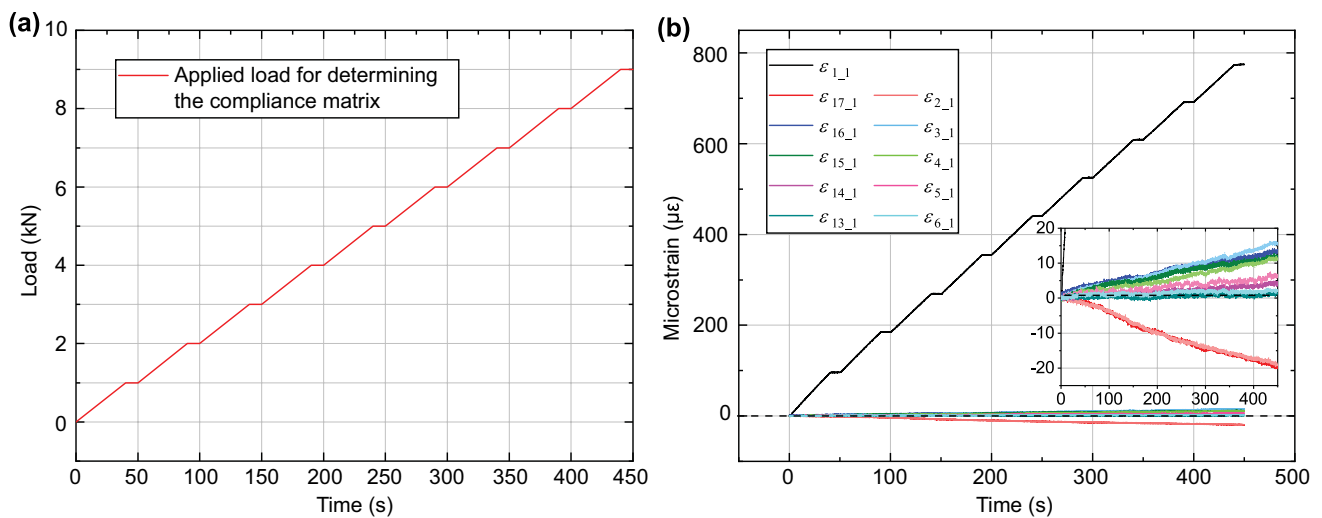
**Fig. 6** **a** The real-time applied load during the calibration matrix test and **b** strain signals from the test when the test point No. 1 is loaded

## 4.2 Measured real-time bearing load

A part of the strain signal $\varepsilon_{12}(t)$ from test position No. 12 under the condition of input speed 1550 rpm and input torque 3000 N·m is intercepted as an example and displayed in Fig. 7a. A magnified view of a section of the strain signal shows five roller revolution cycles in Fig. 7b. Corresponding to 17 rollers of test bearing passing this specific strain gauge position in a roller revolution cycle, each cycle consists of 17 strain pulses with a very similar pulse shape but various peak values which are caused by dynamic contact load between the rollers and outer raceway. The data processing procedure from measured real-time strain signals to time series of roller–raceway contact load contains two steps.
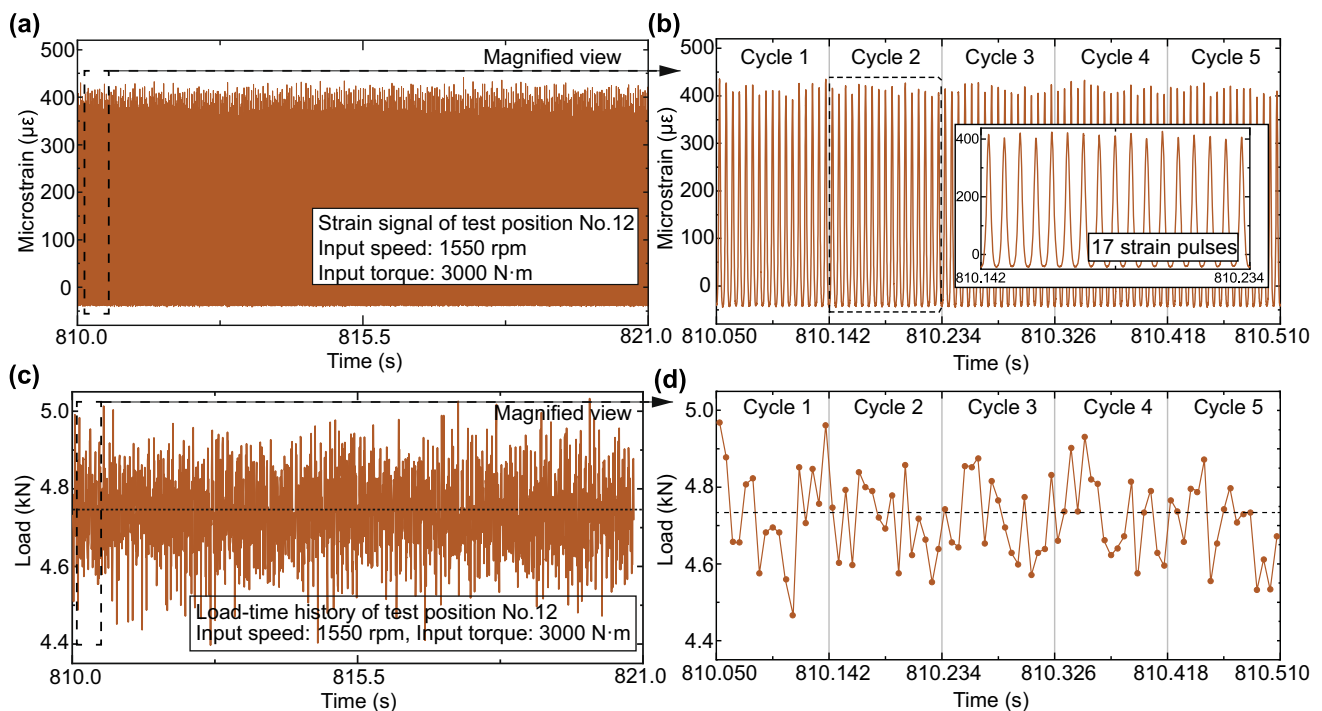


**Fig. 7** Typical measured strain signal and contact load time history obtained accordingly of the test position No.12 under conditions of input speed 1550 rpm and input torque 3000 N·m: **a** measured strain signal; **b** magnified view of the strain signal; **c** measured real-time distributed contact load; **d** a magnified view of the contact load time history
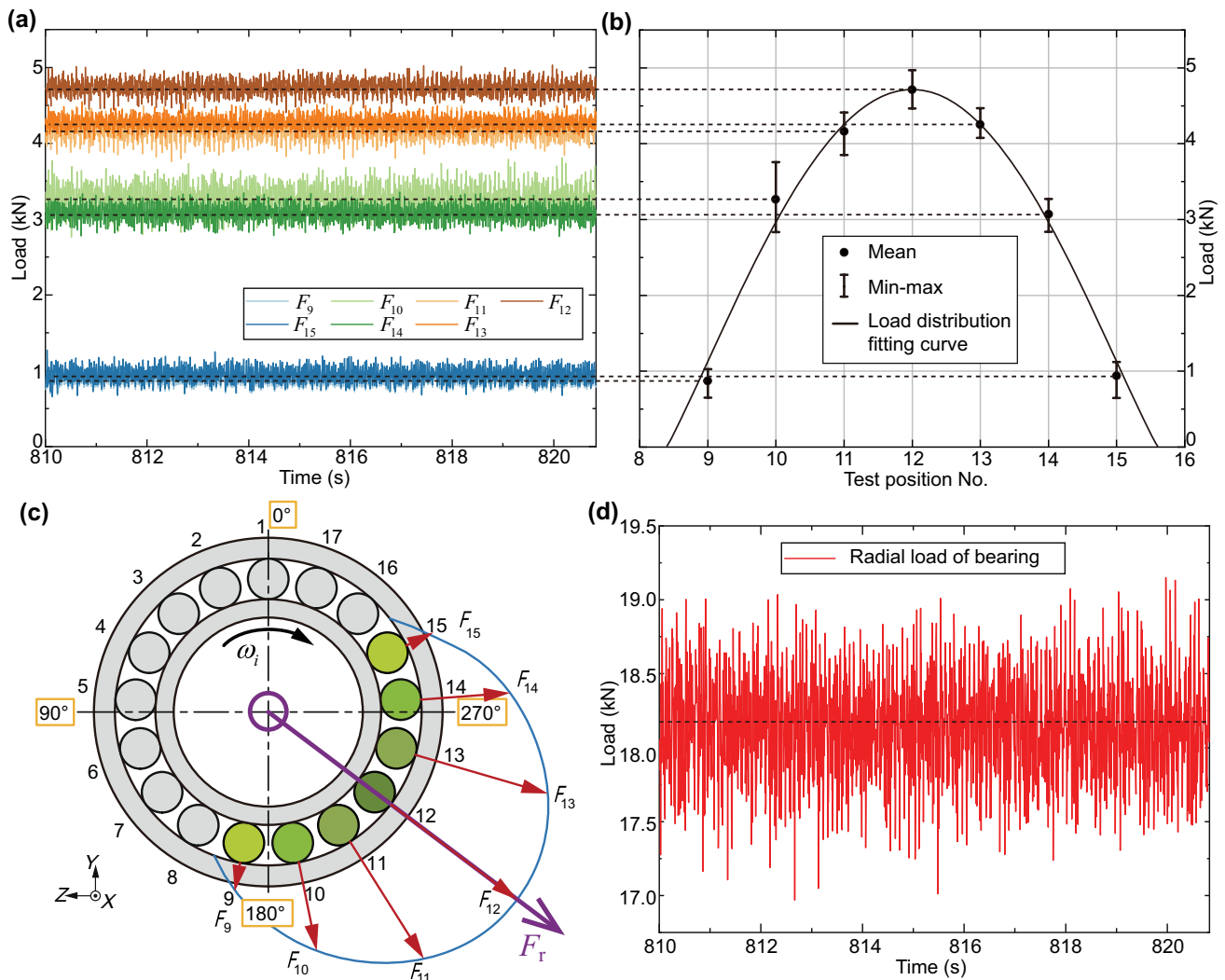
**Fig. 8** Determination of the time history of the measured bearing load (test condition: input speed 1550 rpm and input torque 3000 N·m): **a** typical load time histories of measured nonzero distributed loads; **b** measured load distribution within the bearing; **c** direction of the distributed and total radial load; **d** measured real-time bearing load

First, the time series of peak values of the measured strain signal from all sensing positions are extracted to construct the strain distribution matrix $\boldsymbol{\varepsilon}_\alpha(t)$ in Eq. (1). Second the time series of roller–raceway contact loads distributed on different azimuths are determined by Eq. (1) based on the strain distribution matrix $\boldsymbol{\varepsilon}_\alpha(t)$ and the compliance matrix $\boldsymbol{K}_{\alpha\_\beta}$. Accordingly, the real-time dynamic distributed contact load $F_{12}(t)$ can be obtained and the result is shown in Fig. 7c. It should be noted that the compliance matrix in Eq. (1) is determined when the bearing is stationary and the roller is in the center of each notched region as shown in Fig. 4e, which corresponds to the peak position in cyclic strain response when the bearing rotates. Therefore, the time series of peak values of the strain pulse were used in Eq. (1) to calculate the roller–raceway contact load. In Fig. 7c, the dynamic contact load distributed on this outer raceway position is

observed to irregularly fluctuate around the mean value of 4.73 kN with a range about 0.6 kN. In Fig. 7d, a magnified view of the real-time contact load $F_{12}(t)$ in five roller revolution cycles indicates the variation of the contact load among rollers and cycles. This variation of roller–raceway contact load is considered as a comprehensive result of roller size deviation [24], gear meshing excitation and structural vibration [14].

Figure 8a shows the time histories of all measured nonzero contact loads under the gear meshing condition of input speed 1550 rpm and input torque 3000 N·m. Accordingly, the load distribution within the instrumented bearing is determined and shown in Fig. 8b and c. The points and bounds in Fig. 8b represent, respectively, the mean value and minimum to maximum range of dynamic roller–raceway contact loads shown in Fig. 8a. Besides, the load distribution

🌀 Springer

Rail. Eng. Science (2023) 31(1):37–51
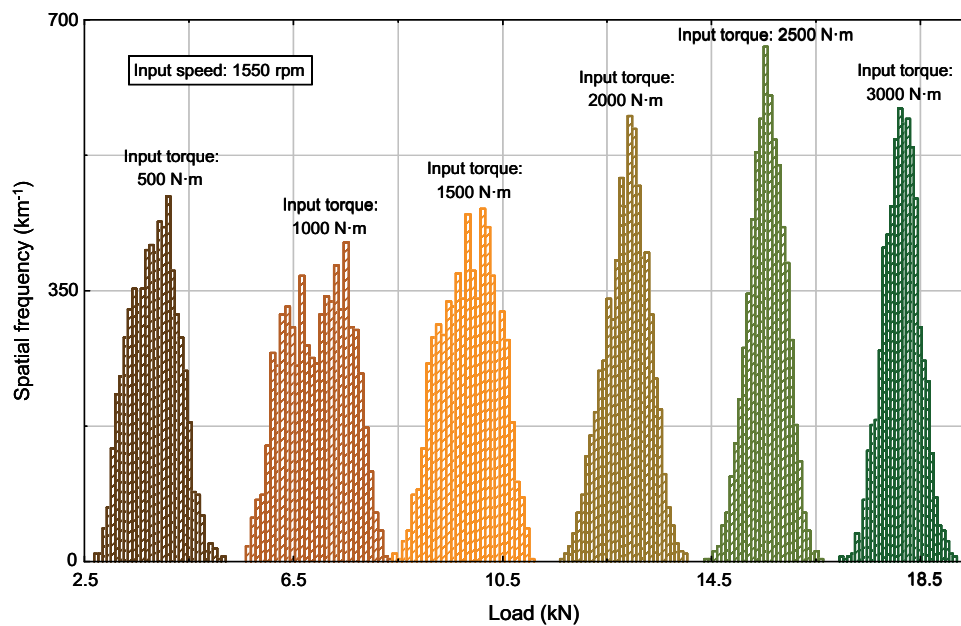
**Fig. 9** Frequency distribution histograms of the measured bearing load under different torque conditions of gear meshing (input speed: 1550 rpm)

curve in Fig. 8b is fitted based on the points according to the Harris theory of bearing radial load distribution [27]. Under this specified condition, the load zone contains seven test positions and the maximum contact load is $F_{12}(t)$. Moreover, the maximum contact load $F_{12}(t)$ is located in the center of the loaded zone while contact loads on either side of the load $F_{12}(t)$ show an axisymmetric distribution with respect to the direction of the load $F_{12}(t)$. Thus, according to Harris theory of bearing radial load distribution [27], the direction of the total radial load $F_r(t)$ of the test bearing is precisely the direction of $F_{12}(t)$, while the real-time amplitude of the total radial load can be obtained by Eq. (2). Figure 8d shows a section of the measured real-time total radial load $F_r(t)$ with a mean value about 18.19 kN and a variation range about 2 kN under this specified condition. For other conditions of gear meshing, the measured load time histories of the instrumented bearing can be determined similarly and then the load spectra of the bearing load under these experimental conditions can be compiled.

### 4.3 Measured load spectra of the gearbox bearing under different conditions

Frequency distribution histograms of the measured bearing load under the two series of gear meshing conditions are, respectively, shown in Figs. 9 and 10. Load spectra of 32-step classification are compiled here according to the Sturges formula [28]. Furthermore, to compare the characteristics of the load spectra under different conditions with the same sample size and classification number of the histogram, the statistical parameter, spatial frequency, is used here, which refers to the count of a certain range of load carried by the gearbox bearing for each kilometer of the train running. The spatial frequency is determined by the input speed, transmission ratio and wheel diameter which is assumed to be 830 mm in this paper.

As shown in Figs. 9 and 10, the load spectra under most of the gear meshing conditions approximately conform to the normal distribution. However, under some conditions, such as the condition of input speed 1550 rpm and input torque 1000 N·m, the frequency distribution of the load spectra is different from the others. Two peaks of spatial frequency appear under these conditions. To characterize the influence of gear meshing conditions on the load spectra of the gearbox bearing, the mean value and class interval of the frequency load spectra under different conditions are, respectively, presented in Figs. 11 and 12. Due to the fixed classification of load spectra under different gear meshing conditions, the class interval represents the discrete degree of the dynamic load of the gearbox bearing.

The mean values of the measured bearing load varying with the test input torque are shown in Fig. 11a. Under conditions of a fixed input speed, the bearing loads increase linearly with input torque as the gear mesh forces increase linearly with torque. In most previous experimental studies, the load of a shaft bearing in a gear transmission system without external excitation was believed to be decided by the shaft bending moments and gear meshing torque as the
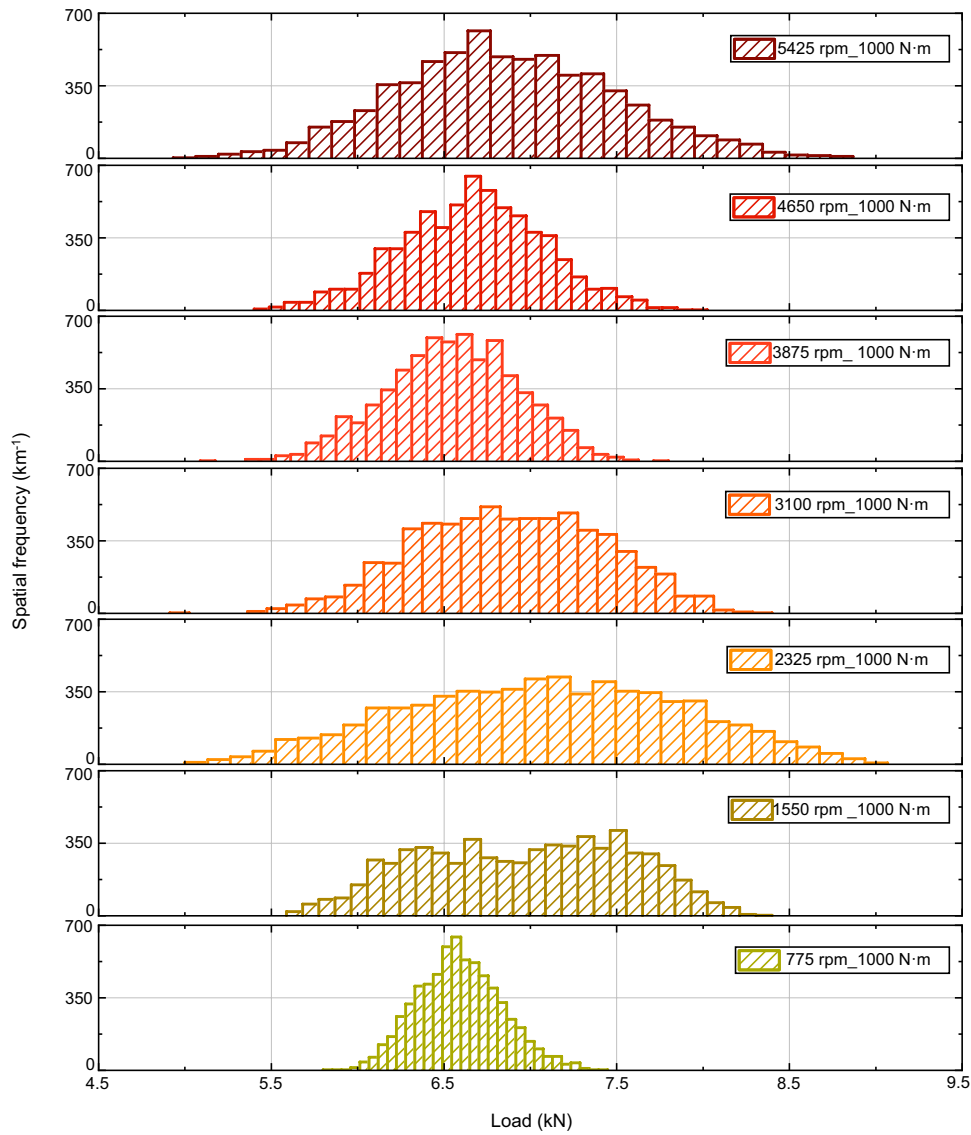
**Fig. 10** Frequency distribution histograms of the measured bearing load under different speed conditions of gear meshing (input torque: 1000 N·m)
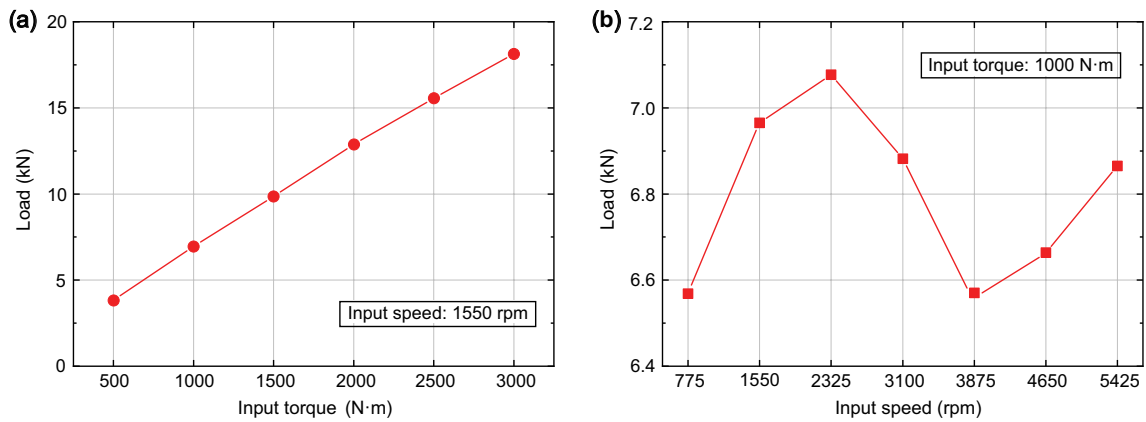


**Fig. 11** Mean values of the measured bearing load under conditions of **a** different torques and **b** different speeds
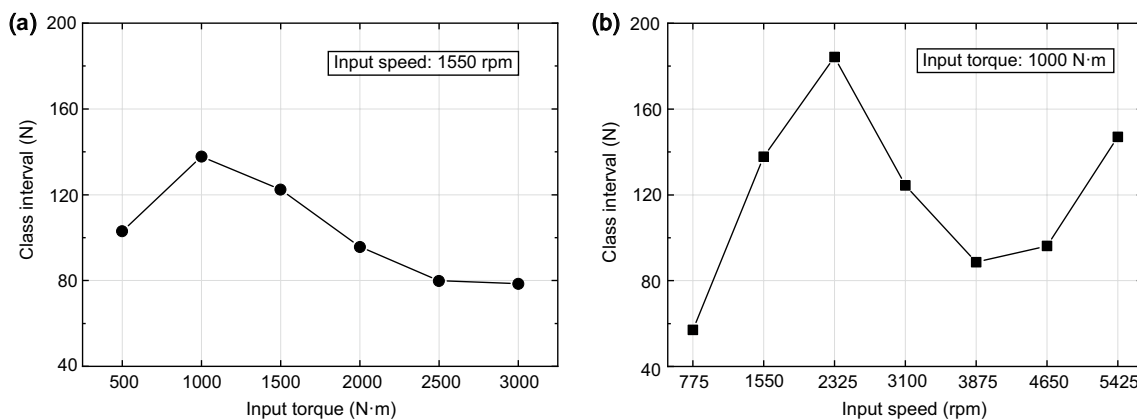
**Fig. 12** Class intervals of the measured bearing load spectra under conditions of **a** different torques and **b** different speeds
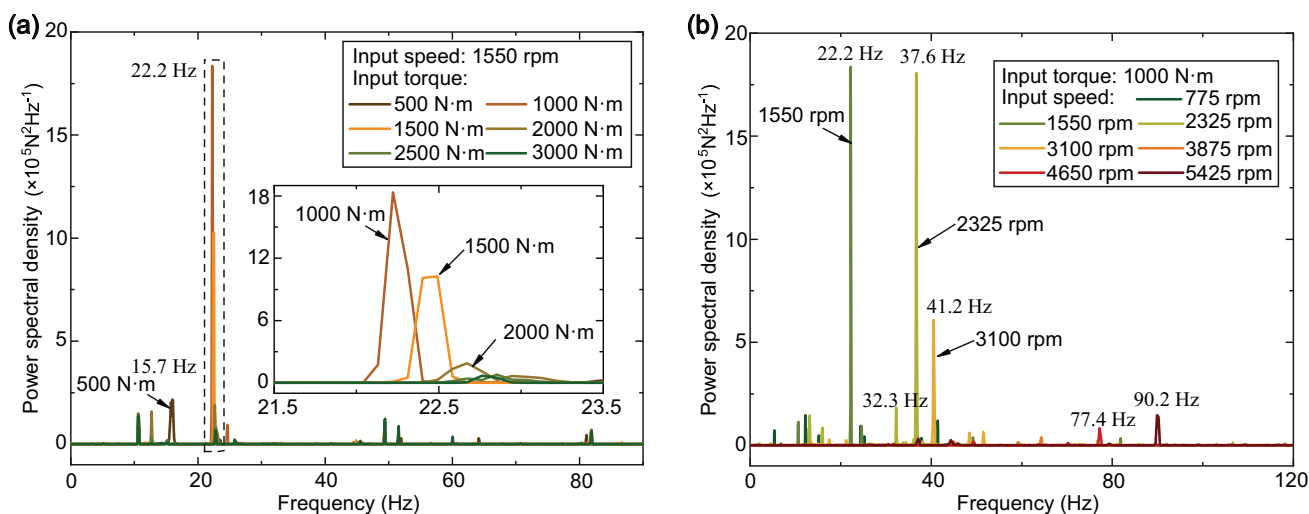


**Fig. 13** Frequency components of the measured bearing load under conditions of **a** different torques and **b** different speeds

**Table 2** The shaft frequency and measured cage frequency under different input speeds

| Input speed (rpm) | High-speed shaft frequency (Hz) | Measured cage frequency (Hz) |
|---|---|---|
| 775 | 12.9 | 5.5 |
| 1550 | 25.8 | 10.9 |
| 2325 | 38.7 | 16.3 |
| 3100 | 51.6 | 21.7 |
| 3875 | 64.5 | 27.0 |
| 4650 | 77.4 | 32.4 |
| 5425 | 90.3 | 37.6 |

effect of the rotational speed on the bearing load was usually small enough to be ignored [19, 21, 24]. Some modeling or simulating research considered the rotational speed as

a factor of the bearing load, which affected the gear mesh force and further the bearing load with a monotonous slight trend under fixed torque conditions [20]. Interestingly, differing from previous results about the effect of speed on the bearing load in the literature, for the test gearbox bearing of high-speed train, a fluctuation of the average load with rotational speed is observed in Fig. 11b. When the input torque is fixed at 1000 N·m, the mean value of the measured bearing load increases initially, followed by a decrease, but then again increases with the increase of the rotational speed. The same trend is reflected in the variation of load spectrum class interval with input speed in Fig. 12b. Besides, as shown in Fig. 12a, the influence of torque on the class interval of the measured bearing load spectra shows a nonmonotonic trend as well. Overall, the characteristics of the measured load spectra of high-speed train gearbox bearing

Rail. Eng. Science (2023) 31(1):37–51

 Springer

for test under different conditions of gear meshing can be drawn as follows:

(1)  The average level of the bearing load is mainly determined by torque, and affected by rotational speed under the condition of a specific torque.
(2)  The class interval of the measured bearing load spectrum varies non-monotonously with torque and speed, which means that the torque and speed of gear meshing are not the direct cause of the dispersion of the measured bearing load spectrum.

To clarify the mechanism of the non-monotonic variation of the measured load spectrum characteristics with the torque and speed of gear meshing, the frequency spectra of the measured time history of bearing load under different conditions are shown in Fig. 13. In Fig. 13a, when the input speed is fixed at 1550 rpm, there are several obvious frequency components under the torque of 500, 1000, 1500 and 2000 N·m. The power of these frequency components varies with torque following the same trend of the class interval with torque presented in Fig. 12a. Under the conditions of constant-torque, the consistency of the various trends of frequency component power and load spectrum characteristics with speed is indicated in the comparison between Figs. 11b, 12b and Fig. 13b. Table 2 provides the rotational frequency of the high-speed shaft and cage under different input speeds. The shaft frequency is calculated by the input speed while the cage frequency is obtained by using a method based on the analysis of measured strain signals [29]. Comparing the frequency components of the measured bearing load in Fig. 13 with the characteristic rotational frequencies of the bearing listed in Table 1, it can be found

that these obvious frequency components of the measured bearing load mostly correspond to the rotation frequency of the high-speed shaft or 2 times the harmonic frequency of the cage rotation. For example, under the speed of 1550 rpm and torques of 1000, 1500 and 2000 N·m, the frequency components about 22.2 Hz shown in Fig. 13a are close to 2 times the harmonic frequency (i.e., 21.8 Hz) of the cage rotation. In Fig. 13b, under the speed of 2325 rpm, the frequency 32.3 Hz is close to 2 times the harmonic frequency (i.e., 32.6 Hz) of the cage rotation while 37.6 Hz is close to the rotational frequency 38.7 Hz of the shaft. It is difficult to say with certainty what causes these obvious frequency components. However, the following evidence from Fig. 13 strongly suggests that it is caused by the in-situ modal vibration of the high-speed shaft or the cage in the bearing:

(1)  The obvious frequency component only appears under some combined conditions of specific speed and torque.
(2)  The vibration of the rotor and the resonance effect induced by the characteristic vibration of cage will arise under specific critical conditions and increase the dynamic response of the bearing [30].

In summary, the non-monotonic variation of the measured load spectrum characteristics is believed to be caused by the vibration of the high-speed shaft or the bearing cage under some combined conditions of specific speed and torque.

### 4.4 Bearing life assessment based on measured load spectra

According to some theories of bearing life [10, 31, 32], an accurate prediction of bearing life needs the input of realistic
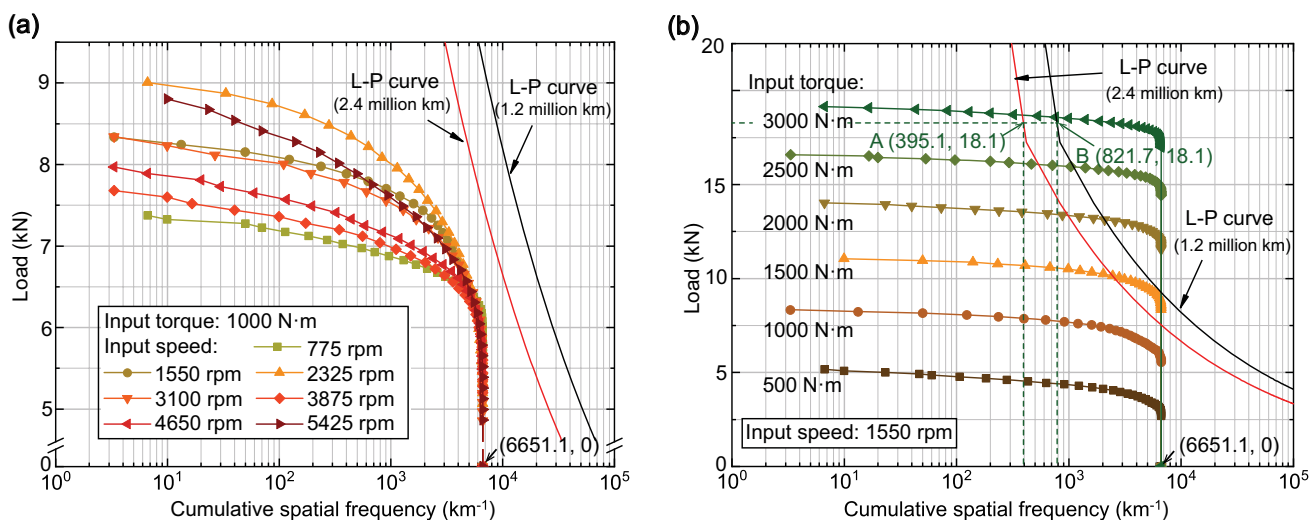


**Fig. 14** Measured cumulative frequency amplitude spectrum of the bearing load under different gear meshing conditions of **a** different speeds and **b** different torques

service bearing loads. In previous research, due to the difficulty of measuring the actual bearing loads and their variations, the load of a shaft bearing in a gearbox was frequently assumed to be a constant load under a specified condition and calculated by using analytical models [19–21, 33]. Compared with the analytical bearing load, the measured load spectrum in this paper can be used to predict gearbox bearing life more realistically.

The gearbox bearing maintenance duration in China is 1.2 million km operation of the train and the scrapping duration is 2.4 million km. Thus, to assess the bearing life using the measured load spectrum, two L-P curves, respectively, corresponding to 1.2 and 2.4 million km operating gearbox bearings are obtained according to Lundberg–Palmgren theory [10] as illustrated in Eq. (5) and given in Fig. 14.

$$L = \left(\frac{C}{P}\right)^p, \tag{5}$$

where $C$ is the basic dynamic load rating of the bearing and equal to 13.7 kN for the test bearing NU214 [34]; $P$ is the bearing load acting under the specified condition and $p = 10/3$ for roller bearings; $L$ is the life in millions of revolutions and has been counted by cumulative spatial frequency in Fig. 14. Besides, the measured cumulative spatial frequency spectrum of the bearing load under different gear meshing conditions is shown in Fig. 14. In Fig. 14a, all of the cumulative frequency–amplitude spectra are below the two L-P curves under the gear meshing conditions of 1000 N·m input torque and different speeds. It means that gearbox bearings operating continuously under such conditions can meet the safe operating requirements of 2.4 million km and perform even better. When the gear meshing speed is fixed, as shown in Fig. 14b, the load spectrum gradually intersects the L-P curve at a smaller cumulative spatial frequency with the increase of gear meshing torque. The damage-equivalent bearing load $F_e$ defined by the Palmgren–Miner rule [33] is used here to assess the bearing life. In general, for $k$ loads each operating for $N_k$ revolutions, the damage-equivalent load $F_e$ is given by

$$F_e = \left[\frac{\Sigma(F_k^p N_k)}{N}\right]^{\frac{1}{p}}, \tag{6}$$

where $F_k$ is the $k$th load component in the measured load spectrum ($k = 1, 2, \ldots, 32$ for the measured load spectra in this paper) and $N$ is the total number of revolutions under one condition of gear meshing. As an example, under the condition of 3000 N·m, the damage-equivalent load of the measured load spectrum is calculated to be 18.1 kN and highlighted by a horizontal dotted line in Fig. 14b. Then, two intersection points A (395.1, 18.1) and B (821.7, 18.1) of the horizontal dotted line and the L-P curves are determined.

According to the damage-equivalent principle [33], intersection points A or B, respectively, represent that to ensure the safe operation of 2.4 or 1.2 million km of the gearbox bearing, the operation time of gearbox under the condition of 3000 N·m input torque should not exceed 5.94% (equal to 395.1/6651.1) or 12.35% (equal to 821.7/6651.1) of the total operation time. Similarly, the limited time of safe operation under other conditions can be obtained. Furthermore, once the gearbox operating conditions in the actual operation process of high-speed train are recorded, the actual life and damage of the gearbox bearing can be accurately predicted and evaluated according to the combination of the measured load spectrum under each operating condition.

### 4.5 Implications and limitations

The implication of the proposed approach in measuring the load spectrum of gearbox bearing has a number of assumptions and limitations.

To measure the load distribution of the gearbox bearing, the same number of notches as the number of rollers were introduced to the test bearing housing circumferentially. It has been verified that the number and geometry of notches on the housing could change the local stiffness of bearings and further the load distribution [35]. To obtain the real load distribution, the introduction of notches must obey the following rules [25]: (1) For a given bearing under an applied load with an unknown direction, the number of notches must be the same as the number of rollers. (2) All the notches should have the same dimension and be evenly distributed on the housing according to the relative position of rollers so that the removal of the material has the same effect for each test position and subsequently no effect on the load distribution.

There are some complexities associated with the installation of the measurement system. The strain gauges are connected to the acquisition equipment by cables. The existence of signal cables increases the difficulty of gearbox assembly. Besides, the presence of an end cover and limited space within the gearbox restrict available regions for cable routing. As a result, some holes were machined on the end cover for leading out the signal cables, which is not allowed for gearboxes in the field. Wireless data acquisition modules based on flexible sensors and integrated circuits are expected to drive the application of this measurement method on gearboxes in the field besides in the test bench.

Notwithstanding the above, this measurement method of bearing load has been successfully applied to load spectrum measurement of bearing in high-speed train gearbox. The measured load spectra of the gearbox bearing under different conditions of gear meshing were compiled for the first time. Furthermore, the measured load spectra of the bearing in high-speed train gearbox can reflect the actual

load conditions and their variations applied on the bearing under different gear meshing conditions, which can be used to monitor the gearbox bearing damage and evaluate the gearbox bearing fatigue reliability.

## 5 Conclusions

In this paper, the load spectra of the bearing in high-speed train gearbox under different conditions of gear meshing were measured and compiled by instrumenting the bearing. Major conclusions are given below:

1. The time histories of the dynamic radial load carried by an instrumented gearbox bearing were deduced from the measured strain signals and a calibrated compliance matrix.
2. Non-monotonic trends of the measured load spectrum characteristics (mean value and class interval) varying with gear meshing speed and torque were found and believed to be caused by the vibration of the high-speed shaft or the bearing cage under some combined conditions of specific speed and torque.
3. Combined with the actual service conditions of the gearbox, the measured load spectrum under different gear meshing conditions can be used to predict gearbox bearing life more realistically.

It should be noted that, besides the gear meshing excitation, the wheel–rail excitation is another significant factor contributing to the load variation and fatigue life of the drivetrain bearing. In future research, the influence of wheel–rail excitation on the gearbox bearing load will be evaluated experimentally. Furthermore, the load spectra of the gearbox bearing under the combined effect of internal gear meshing excitation and external wheel–rail contact excitation will be measured and complied. In addition, the measurement technique of dynamic roller–raceway contact load will be further applied to other drivetrain bearings in high-speed train such as axle box bearings or motor bearings.

## References

1. Hu W, Liu Z, Liu D, Hai X (2017) Fatigue failure analysis of high speed train gearbox housings. Eng Fail Anal 73:57–71
2. Snyder T (2004) Statistical and trend analysis of railroad bearing temperatures. US Patent 6813581, Nov. 2, 2004
3. Zhao D, Gelman L, Chu F, Ball A (2021) Vibration health monitoring of rolling bearings under variable speed conditions by novel demodulation technique. Struct Control Heal Monit 28(2):14–16
4. Entezami M, Roberts C, Weston P et al (2020) Perspectives on railway axle bearing condition monitoring. Proc Inst Mech Eng Part F J Rail Rapid Transit 234(1):17–31
5. Yuan H, Lu C (2017) Rolling bearing fault diagnosis under fluctuant conditions based on compressed sensing. Struct Control Heal Monit 24(5):1–17
6. El-Thalji I, Jantunen E (2015) A summary of fault modelling and predictive health monitoring of rolling element bearings. Mech Syst Signal Process 60–61:252–272
7. Li Y, Liang X, Chen Y et al (2020) Wheelset bearing fault detection using morphological signal and image analysis. Struct Control Heal Monit 27(11):1–15
8. SKF Group (2012) Railway technical handbook volume 2: Drive systems: traction motor and gearbox bearings, sensors, condition monitoring and services. 13085EN: SKF, Sweden
9. Sadeghi F, Jalalahmadi B, Slack TS et al (2009) A review of rolling contact fatigue. J Tribol 131(4):1–15
10. Lundberg G, Palmgren A (1949) Dynamic Capacity of Rolling Bearings. J Appl Mech 16(2):165–172
11. Heuler P, Klätschke H (2005) Generation and use of standardised load spectra and load–time histories. Int J Fatigue 27(8):974–990
12. Wei J, Zhang A, Wang G et al (2018) A study of nonlinear excitation modeling of helical gears with Modification: theoretical analysis and experiments. Mech Mach Theory 128:314–335
13. Wang Z, Cheng Y, Mei G et al (2020) Torsional vibration analysis of the gear transmission system of high-speed trains with wheel defects. Proc Inst Mech Eng Part F J Rail Rapid Transit 234(2):123–133
14. Evans RD, Houpert L, Scandella F et al (2017) Dynamic analysis of rail gearbox bearings. Proc Inst Mech Eng Part F J Rail Rapid Transit 231(8):991–996
15. Wang Z, Zhang W, Yin Z et al (2019) Effect of vehicle vibration environment of high-speed train on dynamic performance of axle box bearing. Veh Syst Dyn 57(4):543–563
16. Wang Z, Allen P, Mei G et al (2020) Influence of wheel-polygonal wear on the dynamic forces within the axle-box bearing of a high-speed train. Veh Syst Dyn 58(9):1385–1406
17. Liu Y, Chen Z, Li W, Wang K (2021) Dynamic analysis of traction motor in a locomotive considering surface waviness on races of a motor bearing. Railw Eng Sci 29(4):379–393
18. Liu Y, Chen Z, Hua X, Zhai W (2022) Effect of rotor eccentricity on the dynamic performance of a traction motor and its support bearings in a locomotive. Proc Inst Mech Eng Part F J Rail Rapid Transit 2022:095440972110723
19. Keller J, Guo Y (2016) Gearbox Reliability Collaborative Investigation of High-Speed-Shaft Bearing Loads. Office of Scientific and Technical Information (OSTI), 2016
20. Guo Y, Keller J (2018) Investigation of high-speed shaft bearing loads in wind turbine gearboxes through dynamometer testing. Wind Energy 21(2):139–150
21. Mcniff B, Guo Y, Keller J, Sethuraman L (2015) High-speed shaft bearing loads testing and modeling in the NREL gearbox

Springer

Rail. Eng. Science (2023) 31(1):37–51

reliability collaborative. In: Paper presented at the Conference for Wind Power Drives, 3–4 March 2015, Aachen, Delaware

22. Keller J, Guo Y, Zhang Z, Lucas D (2018) Comparison of planetary bearing load-sharing characteristics in wind turbine gearboxes. Wind Energy Sci 3(2):947–960

23. Chen W, Mills R, Dwyer-Joyce RS (2015) Direct load monitoring of rolling bearing contacts using ultrasonic time of flight. Proc R Soc A Math Phys Eng Sci 471(2180):20150103

24. Nicholas G, Howard T, Long H et al (2020) Measurement of roller load, load variation, and lubrication in a wind turbine gearbox high speed shaft bearing in the field. Tribol Int 148:106322

25. Hou Y, Wang X (2021) Measurement of load distribution in a cylindrical roller bearing with an instrumented housing: Finite element validation and experimental study. Tribol Int 155:106785

26. Hou Y, Wang X, Que H et al (2021) Variation in contact load at the most loaded position of the outer raceway of a bearing in high-speed train gearbox. Acta Mech Sin 37(11):1683–1695

27. Harris TA, Kotzalas MN (2007) Rolling bearing analysis: essential concepts of bearing technology, CRC Press. Taylor & Francis, Florida

28. Sturges HA (1926) The choice of a class interval. J Am Stat Assoc 21(153):65–66

29. Hou Y, Wang X (2020) Development of an experimental system to measure the cage slip of cylindrical roller bearing. Struct Heal Monit 19(2):510–519

30. Huang D, Liu Y, Liu H, Yi J (2018) Resonances of elastic rotor induced by roller bearing with consideration of cage vibration. Proc Inst Mech Eng Part K J Multi-body Dyn 232(4):446–456

31. Ioannides E, Harris TA (1985) A new fatigue life model for rolling bearings. J Tribol 107:367–377

32. Harris TA, McCool JI (1996) On the accuracy of rolling bearing fatigue life prediction. J Tribol 118:297–308

33. Palmgren A (1959) Ball and Roller Bearing Engineering. Burbank, Philadelphia

34. SKF (2018) Rolling bearings catalogue. 17000 EN, SKF Gr

35. Nagatomo T, Takahashi K, Okamura Y et al (2012) Effects of load distribution on life of radial roller bearings. J Tribol 134(2):1–7